ARTICLES
https://doi.org/10.1038/s41561-022-00903-8
nature geoscience

An initial map of fine-scale heterogeneity in the Earth's inner core

Wei Wang ✉ and John E. Vidale

The seismological properties of Earth's inner core are key to understanding its composition, dynamics and growth history. Within the inner core, fine-scale heterogeneity has previously been identified from backscattering of high-frequency compressional waves. Here we use historical earthquake and explosion data from the Large Aperture Seismic Array, USA, between 1969 and 1975 to build a 3D map of heterogeneity from the inner-core boundary to 500 km depth and determine the geographical distribution of the scatterers across the 40% of the inner core that is visible to the array. Our model has two regions of strong scattering, one beneath eastern Asia and the other beneath South America, both located where past local surveys have identified scattering. We suggest that these loci of strong, fine-scale heterogeneities may be related to random alignments of small, inner-core crystals due to fast freezing. These areas, which have been identified as having high attenuation and lie beneath colder areas of the core–mantle boundary, potentially provide constraints on the dynamics of the inner core and the motions in the outer core, with downwelling in the mantle and outer core possibly associated with strong scattering and inner-core heterogeneity.

Inner-core scattering (ICS, Fig. 1a) was originally identified with data from the Large Aperture Seismic Array (LASA)[1]. More detailed models of the scatterers have subsequently been constructed[2–6]. Some studies indicate that roughness at the inner-core boundary (ICB) and heterogeneity within the inner core contribute to the ICS wave train[2,3]. Determining where the scattering originates and why may be crucial to learning the state and history of the core.

Data analysis

We examined all surviving recordings of earthquakes and explosions from LASA, which ran from 1969 to 1975[7]. LASA comprised up to 525 vertical-component stations across a 200 km aperture, emplaced in 60 m boreholes in firm ground (Supplementary Fig. 1)[8]. We analyse 73 events, reviewed in Peng et al.[4], which include 66 earthquakes and seven explosions, shown in Fig. 1b and listed in Supplementary Table 1. We select the events at the epicentral distances less than 100° from LASA; the ICS waves arriving at greater distances were grazing, more refracted and transmitted, making them harder to interpret, and are weaker and less numerous in the LASA archive.

We bandpass filter the seismograms to retain only 1 Hz to 3 Hz; most energy is 1 Hz to 2 Hz. The ICS energy 2 Hz and above is sufficiently incoherent across the aperture of LASA that it stacks poorly. Arrays with much smaller apertures have examined signals up to 5 Hz (ref. [9]). A beamforming approach including static shift corrections is applied to all the available LASA stations and then envelopes are formed from the time series for each incident wave slowness vector[10]. The static shifts, on the order of tenths of seconds, correct for wavefront distortion due to crust and mantle structures under LASA. The statics were estimated by cross-correlation alignment with iasp91 predictions of the PKiKP phases for an earthquake near the antipode[10]. Use of the statics is critical; without statics, the beam energy is blurred and does not accurately centre on the region in the inner core from which the energy was scattered (Supplementary Fig. 2).

We first measure by beamforming the detectability and accuracy of the inner core-reflected phase PKiKP and the outer core-reflected PcP to calibrate the resolution for the ensuing ICS waves, which span the same range of slownesses. For the explosions, the source duration is short, so we search for PKiKP near the predicted time. In contrast, some of the larger earthquakes have strong energy release lasting for a longer time, so we search for PKiKP arrivals in the first 20 s after the predicted onset, choosing the first well-characterized arrival. Our averaging windows range from 1.5 s to 20 s duration (Supplementary Table 1), depending on the visible signal and noise characteristics. We also form P wave stacks to directly examine the earthquake durations to judge the range of time in which the strongest PKiKP would be expected to arrive for each event, although some P waves are clipped on LASA and thus less diagnostic.

Calibration with PKiKP

We beamform the PKiKP arrivals for all 73 events, finding 50 good, 11 noisy and 12 with no detectable signal (Fig. 1c). We note that about half the PKiKP arrivals for events to the east and southeast are blurred or absent; in other directions, most events show a good PKiKP. Trends versus magnitude, distance and source depth are as expected. They are shown in Extended Data Fig. 1 and are briefly discussed in the supplementary information.

The observed PKiKP beams show good resolution and close agreement with the predicted slowness in Fig. 1d. An example is shown in Supplementary Fig. 3. Most pairs differ by less than 0.005 s km^{-1}. In general, this excellent agreement means that we can directly interpret ICS arrival slownesses to reflect the horizontal location of inner-core scatterers.

There is a tendency on the northwest and southeast edges to have PKiKP observations with up to 0.005 s km^{-1} greater slowness than the predictions. This slight outward mislocation is also apparent in the observed ICS slowness ranges (Extended Data Fig. 2a), which at times extend slightly beyond the expected slowness from the inner core, despite scattering most plausibly originating in the inner core or at the ICB, not in the outer core. To correct such overestimated slownesses close to the slowness of the inner-core rim, we apply a small empirical shift (Methods and Extended Data Fig. 2b).

Department of Earth Sciences, University of Southern California, Los Angeles, CA, USA. ✉e-mail: weiwang053@gmail.com

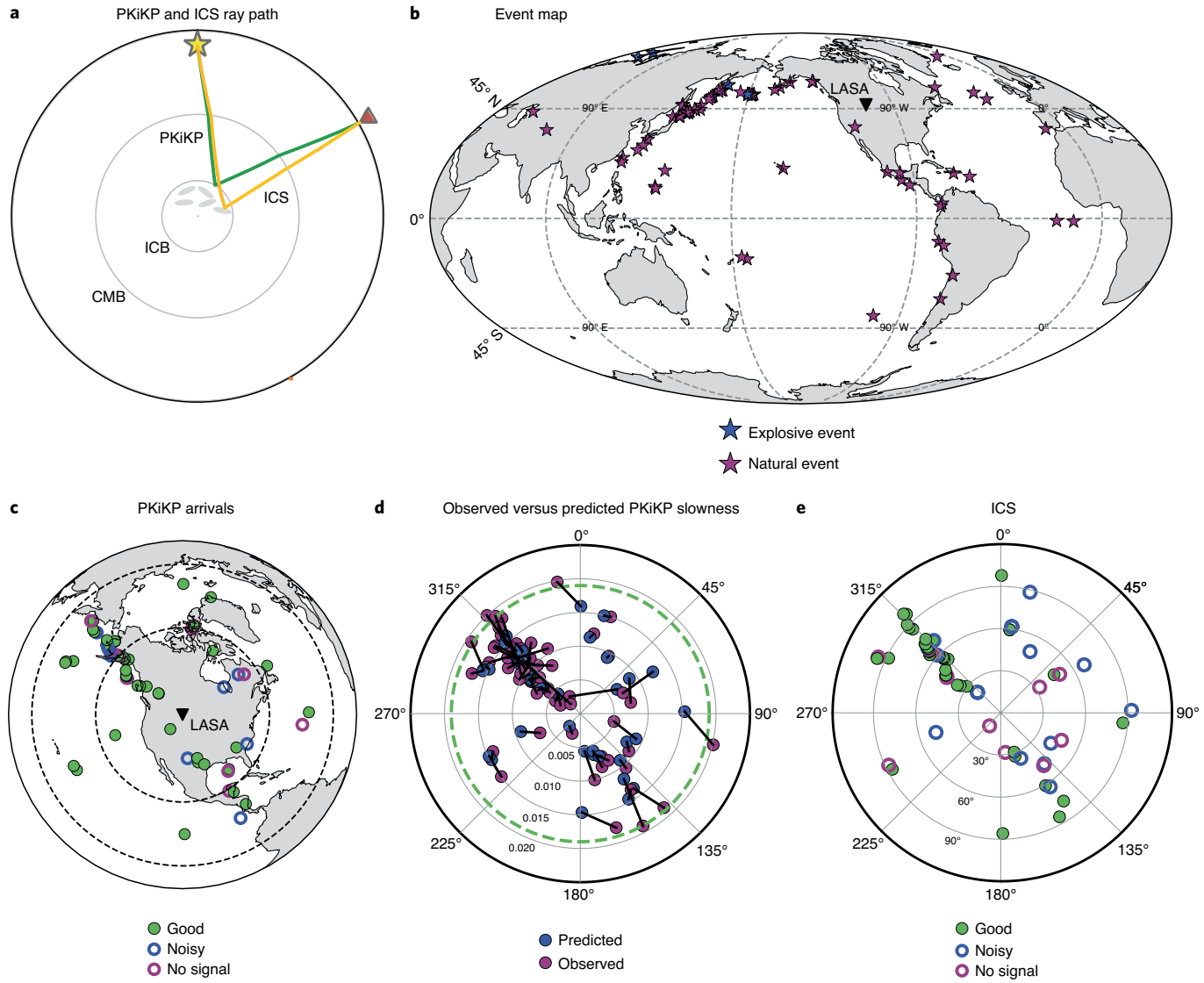

Fig. 1 | Map of events and PKiKP and ICS beam character. a, Cross section showing typical ray paths of PKiKP and ICS. The yellow star shows the event and the orange triangle shows the station. CMB, core–mantle boundary. **b**, Locations of events and the LASA array. **c**, PKiKP quality shown at the location of its ICB bounce point. The inner and outer black dashed lines indicate the 30° and 60° distance from LASA, respectively. **d**, Observed (magenta) versus predicted (blue) slownesses of the 50 well-constrained PKiKP arrivals. Radial axis is total slowness from LASA in s km^{-1}, which can be converted to seconds per degree by multiplying by a factor ~111.19. The transverse axis is back azimuth to the event from LASA. The green dashed circle outlines the rim of slowness grazing the inner core. **e**, ICS character plotted at the corresponding epicentral distance and back azimuth from LASA. LASA is marked by a black triangle in **b** and **c**.

ICS observations

We beamform the seismic waves for the time interval from 20 s to 100 s following the predicted PKiKP time, capturing the strength and slowness of the ICS arrivals at LASA for the 73 events. Most of the ICS lasts many tens of seconds, which is unlikely to be caused by mantle or crust scattering[3]. To resolve the extent of the strong scattering region, we back-project the beamformed ICS envelope to its predicted scatterer location according to slowness vector and lapse time, allowing us to resolve the latitude, longitude and depth of the scatterers (Methods). The spatial resolution of the scattering region degrades with increasing distance to LASA (Supplementary Figs. 4 and 5). Methodological details are given in the Methods and Extended Data Figs. 3 and 4.

Our back-projection approach assumes single scattering. The published ICS models within our studied region have mean free paths longer than 1,500 km according to elastic scattering theory, much longer than our study inner core depth interval (Supplementary Discussion)[1,4,6,11]. If instead there is stronger scattering in the inner core, our resolved depth extent could be deeper than the actual one due to multiple scattering.

Most of the observed ICS at LASA comes from two back azimuths, northeast and southwest. Fig. 2 shows a representative sample of eight beams. The pattern also is reflected in the larger proportion of events with detected ICS to the northwest and southeast in Fig. 1e. Our back-projection reveals that the ICS is caused by two strongly scattering regions within the inner core and perhaps overlying topographically rough patches on the ICB[3]. One region is beneath eastern Asia and the other beneath South America (Fig. 3). The northeastern scattering region extends from the ICB down about 300 km, whereas the southwestern region extends deeper to about 400 km, fading below 500 km.

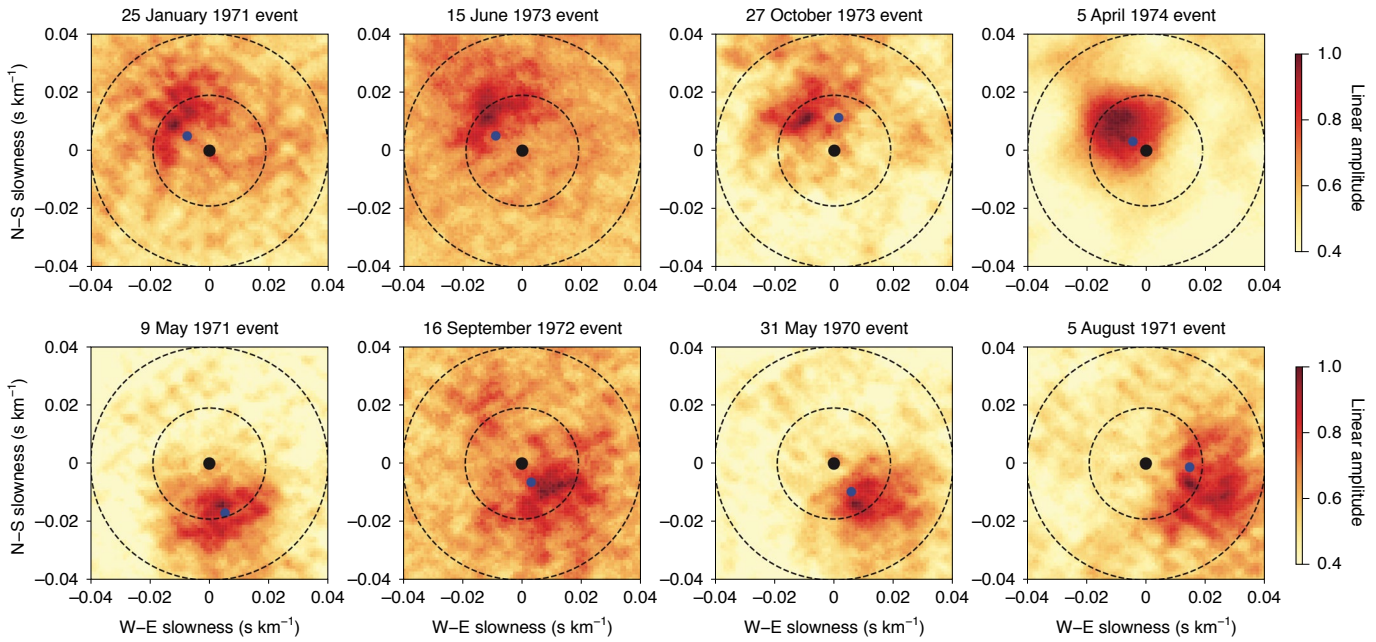

Fig. 2 | Beamforming envelopes summed from 20 s to 100 s after PKiKP for eight events. The blue dots indicate the observed PKiKP slownesses, except for the events on 27 October 1973 and 31 May 1970, for which there are no clear PKiKP arrivals; on those events, we mark the predicted slownesses. The dashed circles indicate the slownesses expected for grazing the inner and outer cores, and the black dot is vertical incidence.

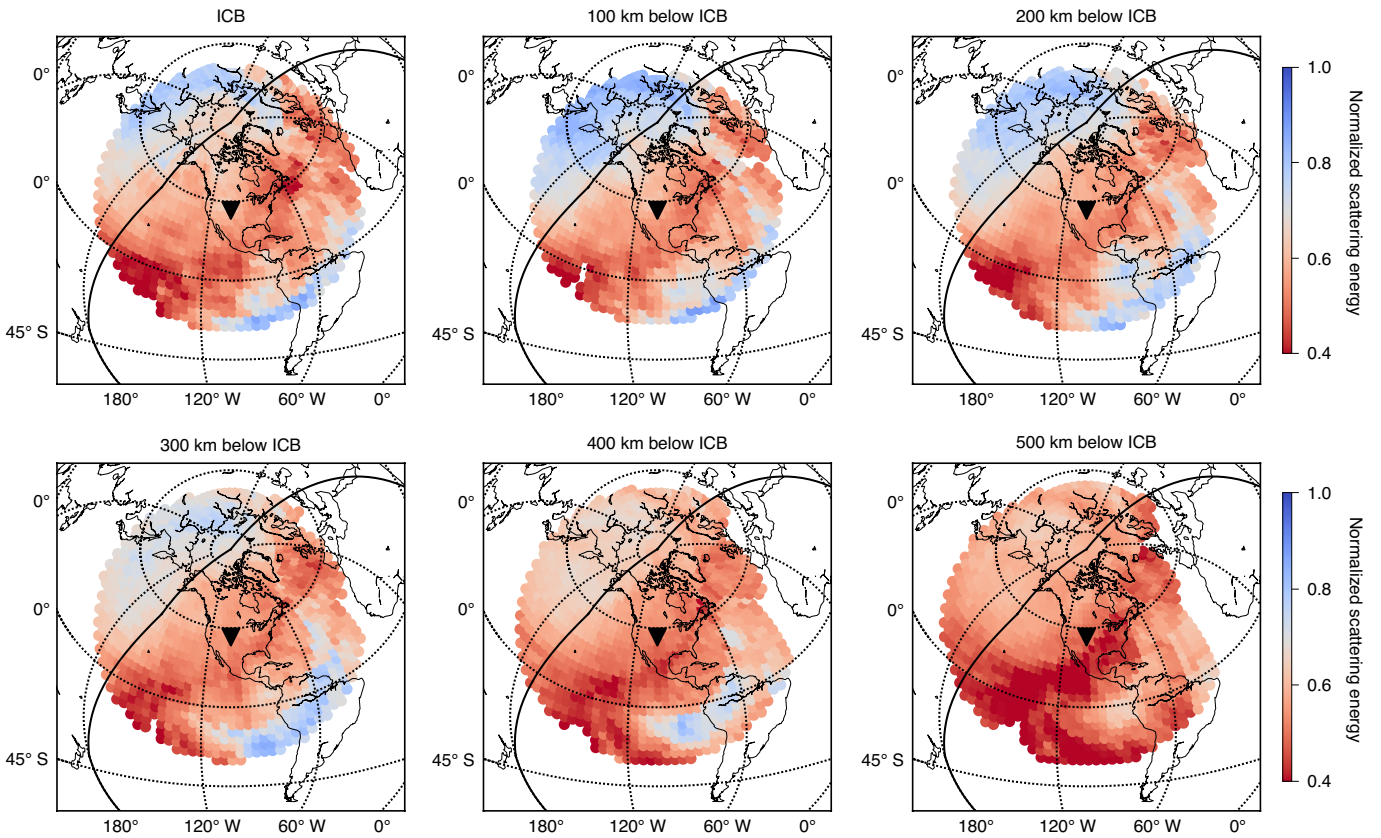

Fig. 3 | ICS strength distribution at various depths below the ICB. LASA is marked by a black triangle. The solid black line shows the eastern–western hemispherical boundary[15].

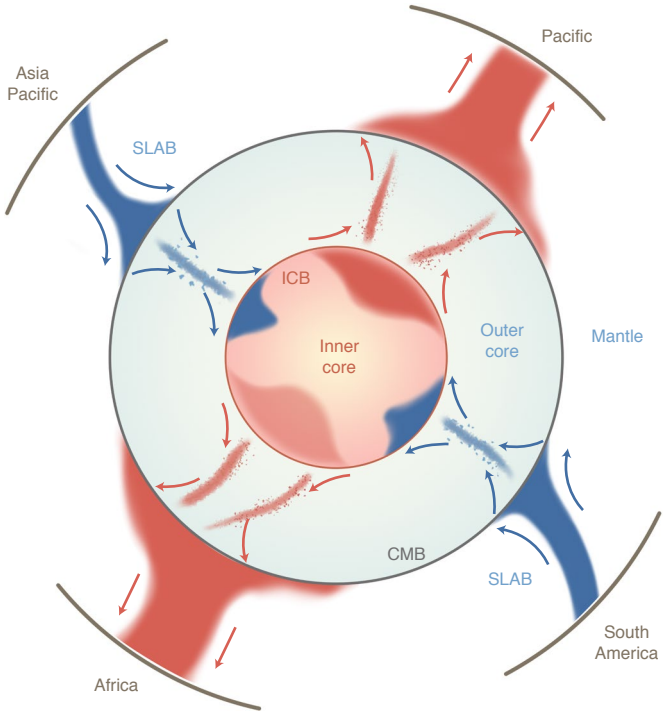

Fig. 4 | Illustration of a possible geodynamic model. The two inner-core regions of strong scattering are aligned with downwellings from the cold regions at the CMB. Weak scattering aligns under the hot CMB beneath the Pacific. We do not image the region under Africa. SLAB, subducting slab.

Discussion

Models of the inner core with radial layering and lateral variation in velocity, anisotropy and attenuation have been developed[12–15]. Lateral variations have a generally hemispheric pattern, with the 'western' hemisphere bounded on the west roughly at 180° W to 160° W and the 'eastern' at 11° E to 60° E. The east side has faster velocity, weaker anisotropy, stronger attenuation and scattering and a thicker outermost isotropic layer than the west[2,5,12–15].

Lateral variations on a smaller scale have also been reported[14,16–21]. Rough ICB topography[18] and a mushy zone[22] are seen atop the strongly scattering region in Asia. Under South America, ICB topography, temporal changes of inner-core shallow structure and shallow scatterers have also been reported in the area we identify as strongly scattering[23,24].

Our findings here are also consistent with previous ICS models, which assumed local or global 1D scattering models. The global observational and numerical studies after our original paper[1] identified more characteristics of ICS. For example, the clearest arrivals are within the distance range 50°–70° (refs. [3,4,9,24,25]). The heterogeneous structure is interpreted to extend to 350 km beneath the ICB, consistent with this paper[3].

The strongly scattering region identified below the Pacific and Asia[4,9] and weakly scattering below America and the Caribbean[6] are consistent with our findings. Because earlier envelope stacks[1,4,6] lack the resolution of our beamforms, these studies have had to assign their 1D models to the PKiKP bounce points rather than the true scattering locations. Recent attenuation tomography of the upper inner core resolves strong attenuation under northern South America and western Asia, roughly consistent with our findings[26], in which the scattering might be a crucial contribution to the attenuation. Areas that this and other studies conclude are more and less anomalous are summarized in Supplementary Fig. 6.

Our study region covers the ~40% of the upper inner core centred at LASA. Two large inner-core regions with strong 1 km- to 10 km-scale heterogeneity with a velocity perturbation about 1% (refs. [1,4]), separated by a large volume with only about half as much velocity perturbation[6], have been identified by our improved beamforming and back-projection technique (Methods). The northwest scattering province extends through the 300 km beneath the ICB, and the South American one extends to 400 km depth.

Multiple physical mechanisms have been suggested to form the fine heterogeneities observed in the inner core. The two strong scattering regions may be due to solidification texturing regulated by the growth rate of inner core. Laboratory experiments show that crystallized hexagonal close-packed metals grow as dendrites[27]. Faster growth results in a less textured solid with more random alignment of hexagonal close-packed preferential orientation and smaller grain size, which may generate more or less backscattering, depending on the scale lengths generated[2,5,28]. Although the crystalline structures of iron in the inner core are still under debate, and other proposed structures, such as the body-centred cubic phase, can be also stable in the presence of light elements in the inner core[29], numerical computation indicates that the seismic energy scattered by those two crystalline structures mostly depends on the grain size rather than the iron structures[5].

Alternatively, compositional variation and a resulting heterogeneity in degree of partial melting could cause the scattering near the ICB. The equation of state of the iron plus light-element eutectic system has a possible range of melting points due to variation in composition[1,22,30,31], or perhaps uneven temperature can be related to convective flow patterns in the outer core[32]. Furthermore, during the evolution of the Earth's inner core, melt may remain trapped within the porosity in the inner core, depending on the rate of compaction and solidification[33,34]. A recent study resolved the melting fraction within the inner core could be as much as a few percentage points, especially in the deep inner core[33], which may be beyond our observation. On the other hand, in the upper inner core, the fraction of the melting might be small due to the more efficient compaction[34]. Consequently, partial melting might be a candidate to explain the ICS.

The spatial distribution of scattering strength in the inner core that we resolve does not match the hemispherical dichotomy that has been resolved by the global studies of inner-core velocity[35] and anisotropy[13,14]. It does share common features with more recent anisotropy models[35] and resembles recent attenuation models[26].

These observations lead us to review the mechanisms proposed to explain large-scale seismic structures in the inner core. The first-order hemispherical patterns in seismic properties have been proposed to arise from a temperature difference between the two sides, perhaps arising from one side of the inner core growing faster than the other side[5,36,37]. Such growth asymmetry might be gravitationally locked to mantle structure and/or it might be internally generated within the inner core. However, the hemispherical dynamics apparently do not preclude the existence of the higher-order structures observed in recent higher-resolution inner-core studies[26,35] and this study.

On the other hand, the heat flux through the core–mantle boundary (CMB) could align the convection in the outer core, controlling the placement of the inner-core structure in a more symmetric degree-two pattern, as suggested by both experiments[38] and geodynamic modelling[28,32,39]. However, other geodynamic simulations suggest stratification just below the CMB would disrupt the dynamics, disconnecting the structure at the CMB and the ICB[40].

The two strong ICS regions that we identify are roughly below the fastest CMB regions in global mantle shear-wave models[41,42], probably marking the coldest places, which would host the highest CMB heat flux (Fig. 4). If the cold downwelling flows mapped radially inward from the CMB, they would cause high heat flux at the ICB. Fast crystallization would result, perhaps causing the observed

pattern of strong scattering[28,43]. In this case, these two strong scattering regions may be critical clues to the thermochemical evolution of the ICB[44].

If inner-core structure does reflect mantle structure, either through gravitational locking or outer core convection coupling, then seismically observed inner-core temporal changes[10,45] would probably be caused by years- to decade-long inner-core oscillations, perhaps as reflected in the six-year variation in length of day[14,46–49] or less regular motion[50]. The inclination of boundaries of the scattering region not yet resolved here could also be a yardstick for inner-core motion relative to the mantle, similar to the geometry of the hemispherical boundary[14].

Online content

Any methods, additional references, Nature Research reporting summaries, source data, extended data, supplementary information, acknowledgements, peer review information; details of author contributions and competing interests; and statements of data and code availability are available at https://doi.org/10.1038/s41561-022-00903-8.

Received: 10 May 2021; Accepted: 16 January 2022;
Published online: 24 February 2022

References

1. Vidale, J. E., Dodge, D. A. & Earle, P. S. Fine-scale heterogeneity in the Earth's inner core. *Nature* **405**, 445–448 (2000).
2. Cormier, V. F. Texture of the uppermost inner core from forward- and back-scattered seismic waves. *Earth Planet. Sci. Lett.* **258**, 442–453 (2007).
3. Leyton, F. & Koper, K. D. Using PKiKP coda to determine inner core structure: 1. Synthesis of coda envelopes using single-scattering theories. *J. Geophys. Res. Solid Earth* **112**, B05316 (2007).
4. Peng, Z., Koper, K. D., Vidale, J. E., Leyton, F. & Shearer, P. M. Inner-core fine-scale structure from scattered waves recorded by LASA. *J. Geophys. Res. Solid Earth* **113**, B09312 (2008).
5. Monnereau, M., Calvet, M., Margerin, L. & Souriau, A. Lopsided growth of Earth's inner core. *Science* **328**, 1014–1017 (2010).
6. Wu, W. & Irving, J. C. E. Using PKiKP coda to study heterogeneity in the top layer of the inner core's western hemisphere. *Geophys. J. Int.* **209**, 672–687 (2017).
7. Hedlin, M. A. H., Earle, P. S. & Bolton, H. Old seismic data yield new insights. *Eos* **81**, 469–473 (2000).
8. Frosch, R. A. & Green, P. E. The concept of the large aperture seismic array. *Proc. R. Soc. A* **290**, 368–384 (1966).
9. Leyton, F. & Koper, K. D. Using PKiKP coda to determine inner core structure: 2. Determination of QC. *J. Geophys. Res. Solid Earth* **112**, B05317 (2007).
10. Vidale, J. E. Very slow rotation of Earth's inner core from 1971 to 1974. *Geophys. Res. Lett.* **46**, 9483–9488 (2019).
11. Sato, H., Fehler, M. C. & Maeda, T. *Seismic Wave Propagation and Scattering in the Heterogeneous Earth* (Springer, 2012).
12. Deuss, A. Heterogeneity and anisotropy of Earth's inner core. *Annu. Rev. Earth Planet. Sci.* **42**, 103–126 (2014).
13. Niu, F. & Wen, L. Hemispherical variations in seismic velocity at the top of the Earth's inner core. *Nature* **410**, 1081–1084 (2001).
14. Waszek, L., Irving, J. C. E. & Deuss, A. Reconciling the hemispherical structure of Earth's inner core with its super-rotation. *Nat. Geosci.* **4**, 264–267 (2011).
15. Yu, W. C. et al. The inner core hemispheric boundary near 180° W. *Phys. Earth Planet. Inter.* **272**, 1–16 (2017).
16. Dai, Z., Wang, W. & Wen, L. Irregular topography at the Earth's inner core boundary. *Proc. Natl Acad. Sci. USA* **109**, 7654–7658 (2012).
17. Cao, A., Masson, Y. & Romanowicz, B. Short wavelength topography on the inner-core boundary. *Proc. Natl Acad. Sci. USA* **104**, 31–35 (2007).
18. Tanaka, S. & Tkalčić, H. Complex inner core boundary from frequency characteristics of the reflection coefficients of PKiKP waves observed by Hi-net. *Prog. Earth Planet. Sci.* **2**, 34 (2015).
19. Ibourichene, A. & Romanowicz, B. Detection of small-scale heterogeneities at the inner core boundary. *Phys. Earth Planet. Inter.* **281**, 55–67 (2018).
20. Wen, L. Localized temporal change of the Earth's inner core boundary. *Science* **314**, 967–971 (2006).
21. Yao, J., Tian, D., Sun, L. & Wen, L. Temporal change of seismic Earth's inner core phases: inner core differential rotation or temporal change of inner core surface? *J. Geophys. Res. Solid Earth* **124**, 6720–6736 (2019).
22. Tian, D. & Wen, L. Seismological evidence for a localized mushy zone at the Earth's inner core boundary. *Nat. Commun.* **8**, 165 (2017).
23. Waszek, L. & Deuss, A. Anomalously strong observations of PKiKP/PcP amplitude ratios on a global scale. *J. Geophys. Res. Solid Earth* **120**, 5175–5190 (2015).
24. Koper, K. D., Franks, J. M. & Dombrovskaya, M. Evidence for small-scale heterogeneity in Earth's inner core from a global study of PKiKP coda waves. *Earth Planet. Sci. Lett.* **228**, 227–241 (2004).
25. Poupinet, G. & Kennett, B. L. N. On the observation of high frequency PKiKP and its coda in Australia. *Phys. Earth Planet. Inter.* **146**, 497–511 (2004).
26. Pejić, T., Hawkins, R., Sambridge, M. & Tkalčić, H. Transdimensional Bayesian attenuation tomography of the upper inner core. *J. Geophys. Res. Solid Earth* **124**, 1929–1943 (2019).
27. Bergman, M. I., Agrawal, S. & Carter, M. S. Transverse solidification textures in hexagonal close-packed alloys. *J. Cryst. Growth* **255**, 204–211 (2003).
28. Aubert, J., Amit, H., Hulot, G. & Olson, P. Thermochemical flows couple the Earth's inner core growth to mantle heterogeneity. *Nature* **454**, 758–761 (2008).
29. Vočadlo, L. in *Treatise on Geophysics* Vol. 2 (eds Price, G. D. & Schubert, G.) Ch. 5 (Elsevier, 2007).
30. Fearn, D., Loper, D. & Roberts, P. Structure of the Earth's inner core. *Nature* **292**, 232–233 (1981).
31. Mao, H. K. et al. Elasticity and rheology of iron above 220 GPa and the nature of the Earth's inner core. *Nature* **396**, 741–743 (1998).
32. Gubbins, D., Sreenivasan, B., Mound, J. & Rost, S. Melting of the Earths inner core. *Nature* **473**, 361–364 (2011).
33. Lasbleis, M., Kervazo, M. & Choblet, G. The fate of liquids trapped during the Earth's inner core growth. *Geophys. Res. Lett*. https://doi.org/10.1029/2019GL085654 (2020).
34. Sumita, I., Yoshida, S., Kumazawa, M. & Hamano, Y. A model for sedimentary compaction of a viscous medium and its application to inner-core growth. *Geophys. J. Int.* **124**, 502–524 (1996).
35. Burdick, S., Waszek, L. & Lekić, V. Seismic tomography of the uppermost inner core. *Earth Planet. Sci. Lett.* **528**, 115789 (2019).
36. Alboussière, T., Deguen, R. & Melzani, M. Melting-induced stratification above the Earth's inner core due to convective translation. *Nature* **466**, 744–747 (2010).
37. Frost, D. A., Lasbleis, M., Chandler, B. & Romanowicz, B. Dynamic history of the inner core constrained by seismic anisotropy. *Nat. Geosci.* **14**, 531–535 (2021).
38. Sumita, I. & Olson, P. A laboratory model for convection in Earth's core driven by a thermally heterogeneous mantle. *Science* **286**, 1547–1549 (1999).
39. Aubert, J., Finlay, C. C. & Fournier, A. Bottom-up control of geomagnetic secular variation by the Earth's inner core. *Nature* **502**, 219–223 (2013).
40. Davies, C. J. & Mound, J. E. Mantle-induced temperature anomalies do not reach the inner core boundary. *Geophys. J. Int.* **218**, 2054–2065 (2019).
41. French, S. & Romanowicz, B. Broad plumes rooted at the base of the Earth's mantle beneath major hotspots. *Nature* **525**, 95–99 (2015).
42. Garnero, E., McNamara, A. & Shim, S. H. Continent-sized anomalous zones with low seismic velocity at the base of Earth's mantle. *Nat. Geosci.* **9**, 481–489 (2016).
43. Venet, L., Duffar, T. & Deguen, R. Grain structure of the Earth's inner core. *C. R. Geosci.* **341**, 513–516 (2009).
44. Deguen, R. & Cardin, P. Tectonic history of the Earth's inner core preserved in its seismic structure. *Nat. Geosci.* **2**, 419–422 (2009).
45. Song, X. & Richards, P. G. Seismological evidence for differential rotation of the Earth's inner core. *Nature* **382**, 221–224 (1996).
46. Mound, J. & Buffett, B. Detection of a gravitational oscillation in length-of-day. *Earth Planet. Sci. Lett.* **243**, 383–389 (2006).
47. Ding, H. & Chao, B. F. A 6-year westward rotary motion in the Earth: detection and possible MICG coupling mechanism. *Earth Planet. Sci. Lett.* **495**, 50–55 (2018).
48. Souriau, A. in *Treatise on Geophysics* Vol. 1 (eds Price, G. D. & Schubert, G.) Ch. 19 (Elsevier, 2007).
49. Roberts, P. H. & Aurnou, J. M. On the theory of core-mantle coupling. *Geophys. Astrophys. Fluid Dyn.* **106**, 157–230 (2012).
50. Tkalčić, H., Young, M., Bodin, T., Ngo, S. & Sambridge, M. The shuffling rotation of the Earth's inner core revealed by earthquake doublets. *Nat. Geosci.* **6**, 497–502 (2013).

Methods

The empirical correction of PKiKP slowness. The PKiKP slowness observations are consistent with the predictions within 0.0025 s km^{-1}, on average, as shown in Extended Data Fig. 2 and Supplementary Fig. 4. However, we observe that arrivals predicted to be near inner-core grazing slownesses tend to have slownesses slightly greater than predicted. Figure 1d, Supplementary Fig. 4 and Extended Data Fig. 2a indicate that most of the misfit is radial. Here we form an empirical correction:

$$s_{obs} = \begin{cases} s_{pred} & s_{obs} < s_0 \\ a \times (s_{pred} - s_0) + s_0 & s_{obs} \geq s_0 \end{cases} \quad (1)$$

in which s_{obs} and s_{pred} are observed and predicted slownesses, a is the correction coefficient and s_0 is a critical slowness beyond which we apply an empirical equation (1) to correct the observed slowness. We grid search the parameters a and s_0 to best fit the observations. The relatively larger observed than predicted slownesses are probably caused by the structure in the mantle under LASA. To expand the observed slowness range to better constrain the correction, we also include the slowness misfit of PcP arrivals for the same events. The comparison of different choices of correction (Extended Data Fig. 2b) shows that if we use only the PKiKP data to constrain the correction, it overcorrects PcP misfits. We apply the empirical correction constructed, including PKiKP and PcP data. In the sensitivity studies in the supplementary information, we compare the result of using two other corrections (see Supplementary Figs. 7 and 8).

Array processing and imaging approach. We have developed an improved method to determine the location of ICS based on array measurements. The basic idea is developed and improved from the techniques of Wen[51] and Cao et al.[52] that use beams of PKP precursors to determine the locations of scatterers in the lower mantle. Wen[51] posits that the precursor energy at a specific time before the PKP arrival could arise from anywhere on 'isotime' surfaces in both source- and receiver-side lower mantle (Fig. 3 in Wen[51]). This approach can locate scatterers in three dimensions. The model is refined with data from multiple sources and/or receivers. Next, Cao et al.[52] adds the vector slowness of the precursor energy in addition to its relative time before PKP arrival for each doublet to constrain the scatterer location to a point rather than just anywhere on a surface.

Here we apply a similar technique to detect the strong scattering regions in the inner core with ICS, which are PKiKP coda waves based on the same assumption of single scattering as Wen[51], Cao et al.[52] and Frost et al.[53] (Supplementary Discussion). If scattering occurs in the inner core or on the ICB elsewhere than at the PKiKP bounce point, the ray path is longer than that of PKiKP, so the scattered energy arrives later than PKiKP and appears at a diagnostic slowness and lapse time. Extended Data Fig. 4 shows how the distribution of time delay and slowness of the coda waves correspond to its scattering location.

The beamformed image from each event is the summation of the envelopes of the beams for all the back azimuths and slownesses projected into the inner core (Extended Data Fig. 3). The scattered energy from different inner-core depths appears at resolvable different lapse times and slownesses in the beamformed seismogram. All the beamformed images for individual events are then stacked. Finally, the summed energy at each grid is normalized by the count of contributions to that grid to recover the relative scattered energy (Extended Data Fig. 4).

In this study, we divide the inner core into 4°×4°×50 km cells. We select only the 45 earthquakes with 'good' ICS (Fig. 1e), projecting the energy back to its corresponding scattering location within the inner core. The iasp91 model is used for 1D raytracing. We use the empirical equation (1) above to correct the observed slowness. We estimate the envelope as the median value within a 20 s time window centred at the chosen lapse time. We begin analysis of the ICS signal 5 s after the hand-picked PKiKP ending time (Supplementary Table 1) to minimize mistaking the later part of an extended source duration for ICS. The ending time for our back-projection approach is 100 s after the PKiKP arrival time at which time ICS arrivals are fading into the noise. Later ICS is visible, so our inversion may underestimate deeper scattering.

The resulting spatial map of inner-core scatterers based on LASA data is shown in Fig. 3. Timing uncertainty arises from the length of the window used and the variable source duration of the earthquakes, but even a 10 s difference leads only to an around 50 km change in scatterer depth, which does not affect our conclusions. To assure robustness, we consider only the regions with hit counts larger than three. In the shallow inner core (<300 km), almost all the hit counts are larger than five (Supplementary Fig. 10). Resolution is more limited by estimation of ICS slowness. We plot predicted slowness versus the scatterer distance to LASA in Supplementary Fig. 5. The increasing slope indicates a given error in slowness leads to greater error in depth estimation at greater ranges so that the spatial resolution of the scattering region degrades with increasing distance to LASA.

Data availability

The LASA data are available online (https://github.com/JohnVidale/LASA_data). The events used in this study are listed in Supplementary Table 1.

Code availability

All the code will be available upon request.

References

51. Wen, L. Intense seismic scattering near the Earth's core mantle boundary beneath the Comoros hotspot. *Geophys. Res. Lett.* **27**, 3627–3630 (2000).
52. Cao, A. & Romanowicz, B. Locating scatterers in the mantle using array analysis of PKP precursors from an earthquake doublet. *Earth Planet. Sci. Lett.* **255**, 22–31 (2007).
53. Frost, D. A., Rost, S., Selby, N. D. & Stuart, G. W. Detection of a tall ridge at the core–mantle boundary from scattered PKP energy. *Geophys. J. Int.* **195**, 558–574 (2013).

Acknowledgements

P. Earle recovered the LASA data from deteriorating nine-track tapes in the 1990s, and S. Gibbons provided digital copies from his archives in 2019. Discussions with J. Aurnou, S. Ni, L. Wen and J. Yao were very helpful. This study is supported by National Science Foundation grant EAR-2041892.

Author contributions

W.W. and J.E.V. each contributed equally to project design, methodology, data processing and manuscript preparation.

Competing interests

The authors declare no competing interests.

Additional information

Extended data is available for this paper at https://doi.org/10.1038/s41561-022-00903-8.

Supplementary information The online version contains supplementary material available at https://doi.org/10.1038/s41561-022-00903-8.

Correspondence and requests for materials should be addressed to Wei Wang.

Peer review information *Nature Geoscience* thanks Jessica Irving and the other, anonymous, reviewer(s) for their contribution to the peer review of this work. Primary Handling Editor: Rebecca Neely, in collaboration with the *Nature Geoscience* team.

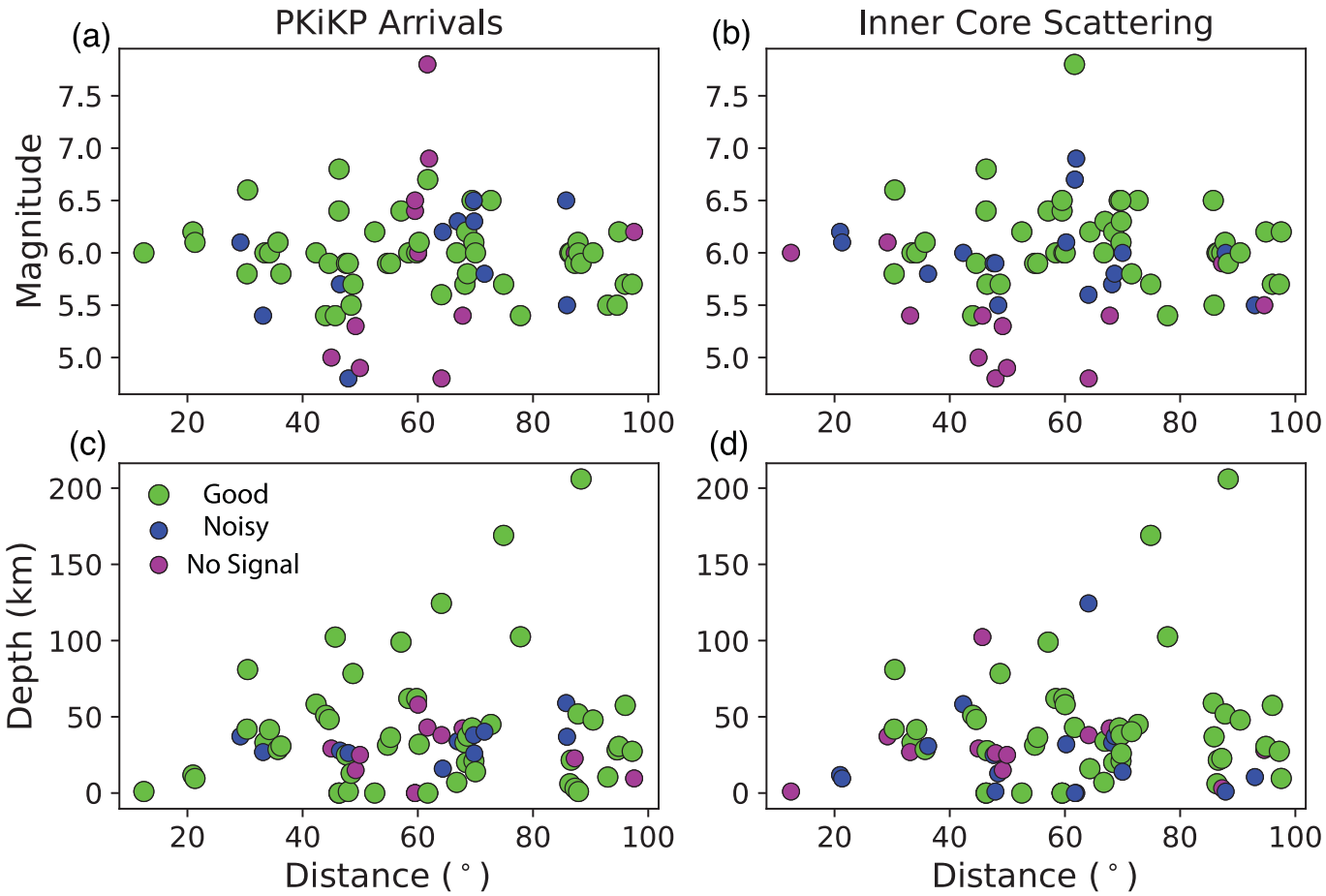

Extended Data Fig. 1 | Observation quality as a function of magnitude and depth vs distance of the 73 events that we analyse. Observation quality as a function of magnitude and depth vs distance of the 73 events that we analyse. PKiKP (a) & (c) and ICS (b) & (d) arrivals rated as "good", "noisy" and "no signal" are shown as green, blue, and magenta dots, respectively.

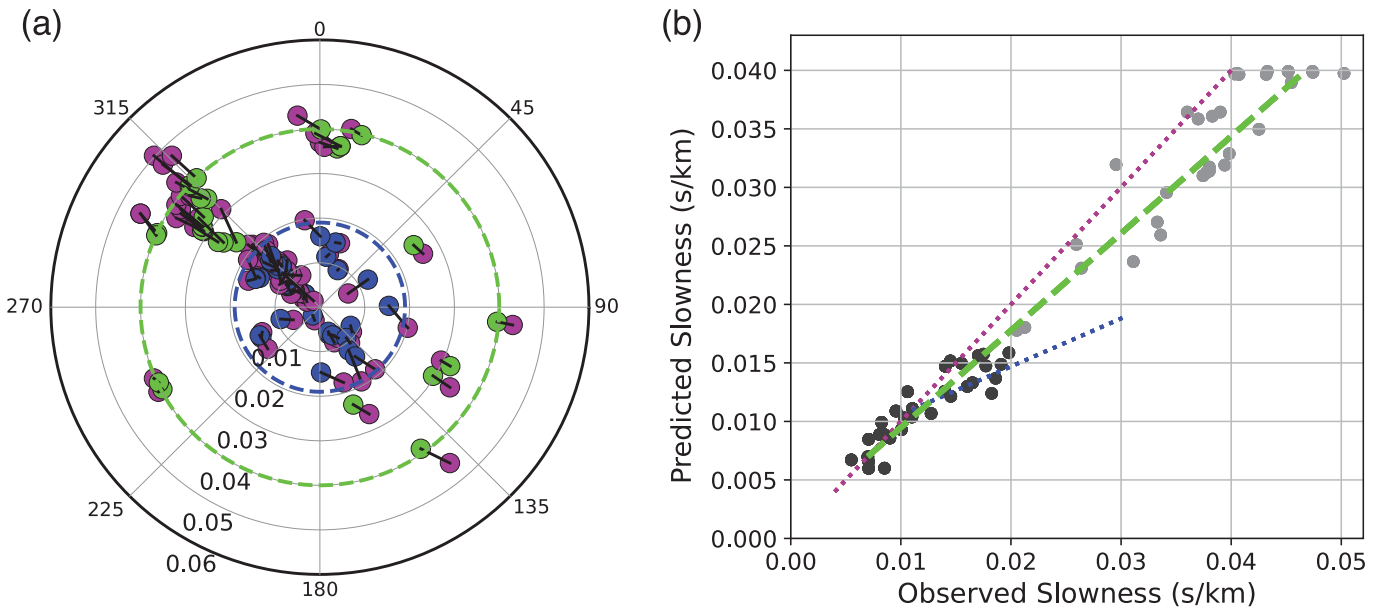

Extended Data Fig. 2 | Comparison of observed vs predicted PKiKP and PcP slownesses for all "good" events and the empirical correction of the slowness. Comparison of observed vs predicted PKiKP and PcP slownesses for all "good" events and the empirical correction of the slowness. (a) Predicted (purple) slownesses of the well-constrained observed PKiKP (blue dots) and PcP (green dots) arrivals. Radial axis is total slowness from LASA in s/km, transverse axis is back-azimuth to the event at LASA. The blue and green dashed circles outline the slownesses of the rims of the inner and outer core, respectively. (b) Empirical correction of the slowness. The black and grey dots are PKiKP and PcP arrivals, respectively. The purple dotted line indicates no correction. The green dashed line ($a = 0.83,\ s_0 = 0.007$) shows the best fitting empirical correction using all PcP and PKiKP arrivals, and blue dotted line ($a = 0.41,\ s_0 = 0.011$) shows the best fitting correction using only PKiKP arrivals.

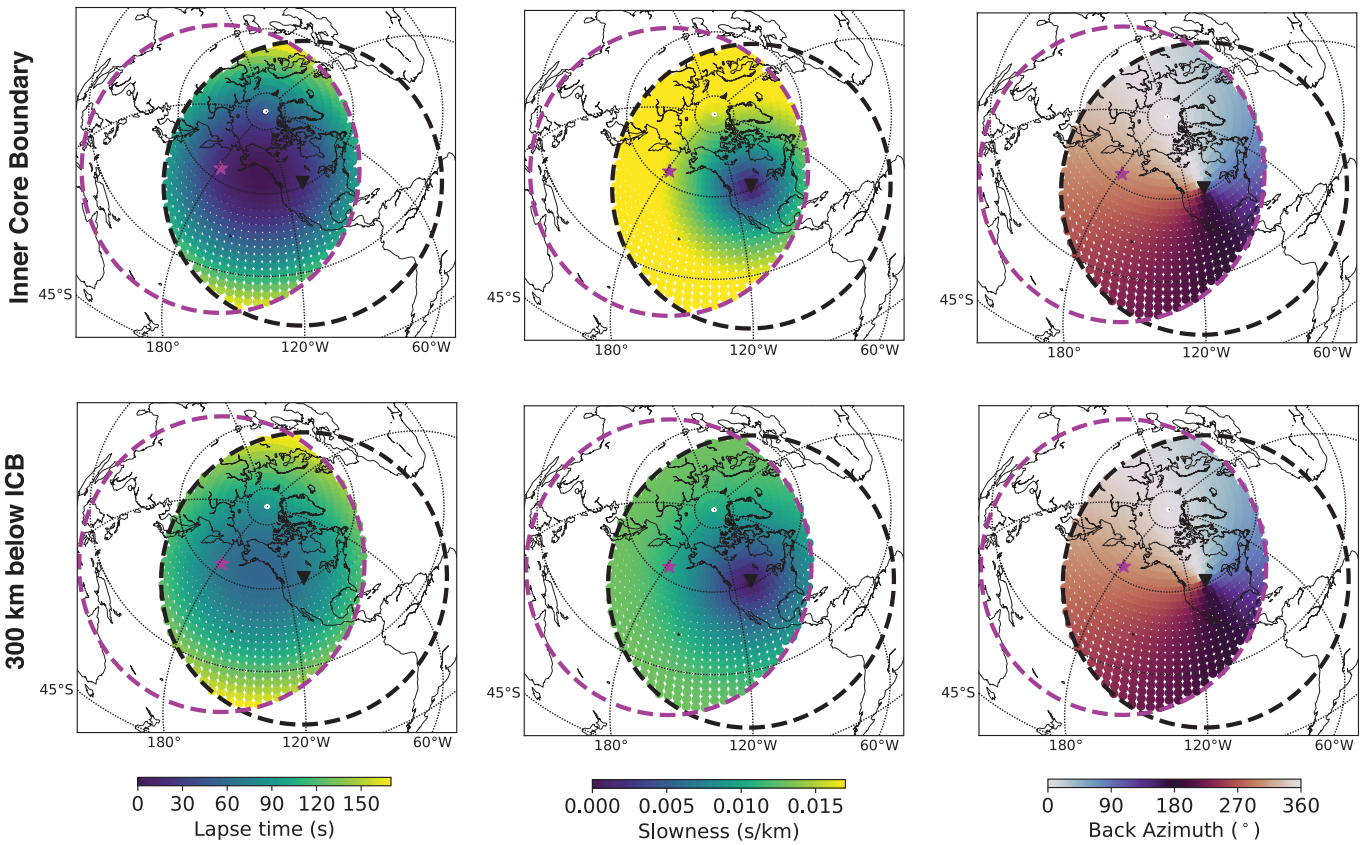

Extended Data Fig. 3 | Lapse time after PKiKP, total slowness, and back azimuth of the scattered waves located across isodepth slices of the IC. Lapse time after PKiKP, total slowness, and back azimuth of the waves scattered across slices at various depths of the IC. The top panel shows results for the scatterers located at the ICB, and the bottom panel shows results for the scatterers located at the depth of 300 km below the ICB. The black triangle shows the location of LASA and black dashed line indicates the outline of IC scatterers that would be visible at LASA from events everywhere. The magenta star indicates the source location, and the magenta dashed line shows the outline of the potential IC scatterers illuminated by this source that would be visible given arrays everywhere.

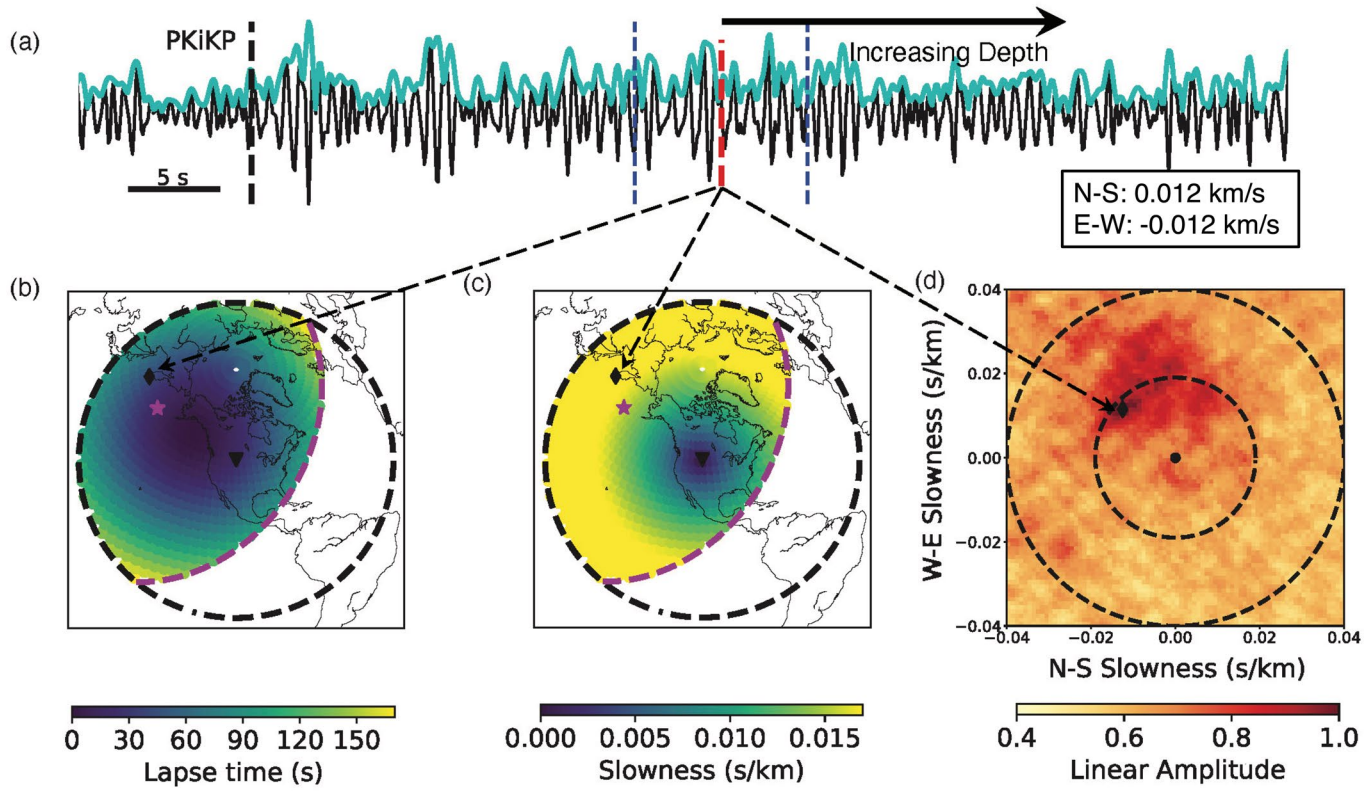

Extended Data Fig. 4 | Illustration of application of the new technique to data. Illustration of application of the new technique to data. This example uses the 11/27/73 event. (a) shows the seismogram (black) and envelope (cyan) from beamforming at N-S slowness 0.012 km/s and E-W slowness −0.012 km/s. The red dashed line marks energy corresponding to a particular scattering volume in the IC and the blue dashed lines delimit the time window used for the energy estimate for that lapse time and slowness vector. (b) and (c) correspond to Extended Data Figs. 3a and 3b, and the black diamond indicates the location of the resolved scatterer. (d) shows the 2D beamforming summation as a function of the slowness vector for the time window 20–100 seconds after PKiKP. The black diamond is the slowness chosen for the illustration in (a), (b), and (c). The two dashed rings indicate the slowness expected for arrivals from the rims of the inner core and outer core.